ISIJ International, Vol. 64 (2024), No. 11, pp. 1705–1715
https://doi.org/10.2355/isijinternational.ISIJINT-2024-174

Microstructure and Mechanical Properties of Gas Metal Arc-welded Fe–Mn–Si Seismic Damping Alloy

Tomoya NAGIRA,[1)]* Terumi NAKAMURA,[1)] Fumiyoshi YOSHINAKA,[1)] Takahiro SAWAGUCHI[1)] and Yasuhiko INOUE[2)]

1) National Institute for Materials Science, 1-2-1, Sengen, Tsukuba, Ibaraki, 305-0047 Japan.
2) Takenaka R & D Institute, Takenaka Corporation, 1-5-1, Ohtsuka, Inzai, Chiba, 270-1395 Japan.

(*Received May 29, 2024; Accepted July 9, 2024; Advance online published July 19, 2024; Published September 15, 2024*)

A brace-type seismic damper made of an Fe-15Mn-11Cr-7.5Ni-4Si alloy solidified in the ferrite-austenite (FA) mode and SN490B steel, which can be constructed via welding, was proposed. To realize the proposed seismic damper, gas metal arc welding was applied to produce similar FMS/FMS fillet welds and dissimilar FMS/SN490B fillet weld joints. Based on the Schaeffler diagram, similar and dissimilar welding consumables were designed such that the fillet weld metal solidified in the FA mode without solidification cracking. Sound similar fillet welded joints were obtained using two types of welding consumables with different Cr/Ni equivalent ratios although both the similar fillet weld metals had a coarse columnar austenite grain structure. These displayed higher tensile strengths (716–736 MPa) and marginally lower elongations (67–70%) than the FMS alloy. Moreover, a similar fillet weld metal with a chemical composition almost identical to that of the FMS alloy exhibited a remarkable low-cycle fatigue life (5 740 cycles). This was shorter than that of the FMS alloy (9 351 cycles) owing to the easier formation of α'-martensite. A dissimilar fillet welded joint with a chemical composition within the austenite region was produced without solidification cracking. The dissimilar fillet weld metal showed high tensile strength (867 MPa) and total elongation (61%). These were comparable to those of similar fillet weld metals.

KEY WORDS: gas metal arc welding; Fe–Mn–Si alloy; seismic damping alloy; fillet weld metal.

1. Introduction

Seismic damper devices including steel and viscous dampers that absorb the vibrations of tall buildings generated by earthquakes[1)] have become increasingly important in Japan, where long-term and long-period ground motion can occur. Recently, an Fe-15Mn-4Si-10Cr-8Ni (FMS) alloy[2)] with a fatigue life 10 times longer than that of conventional low-yield point steel for seismic dampers was developed.[3,4)] The reversible transformation between γ-austenite and ε-martensite under cyclic push–pull loading contributed to the remarkable fatigue life. In 2015, a shear panel FMS alloy seismic damper was installed in a high-rise building in Japan.[1)] The FMS alloy core plate in the seismic damper is connected to the inside- and outside-stiffened plates and a spacer plate with bolted joints. This is because fusion welding is not applicable to FMS alloys, which are vulnerable to solidification cracking owing to austenite (A) mode solidification.[5)] Recently, we proposed a brace-type seismic damper that can be produced using a welding technique, as shown in **Fig. 1**, based on the previously designed one[1)] to enhance the application range of FMS alloys to seismic dampers. The cross-shaped core part of the damper consists

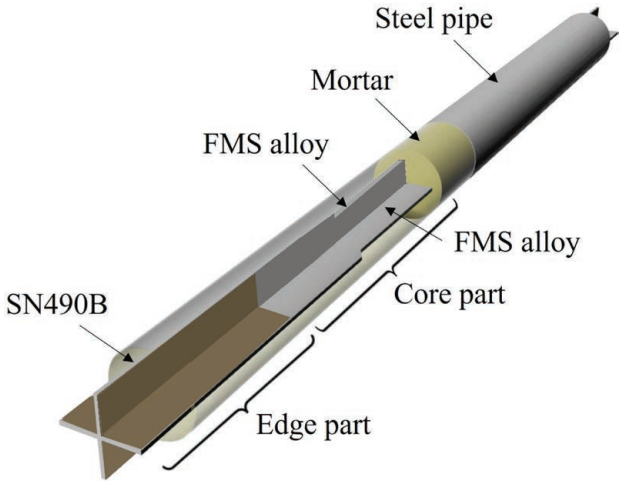

Fig. 1. Schematic of brace-type FMS alloy seismic damper. (Online version in color.)

* Corresponding author: E-mail: NAGIRA.Tomoya@nims.go.jp

of the FMS alloy plates joined by fillet welding. It is joined to the cross-shaped edge part consisting of conventional structural steels (SN490B steel) by welding. Mortar and steel pipes are used to restrain the buckling of core part. Because the core functions as a damping device that absorbs earthquake-induced vibrations, it is necessary to produce a weld joint with a long plastic fatigue life comparable to that of the FMS alloy.

To produce the proposed brace-type seismic damper, a welding technique for joining FMS alloy plates was developed in a previous study.[6] When a fillet welded joint is produced using gas metal arc welding without welding consumables, severe solidification cracking occurs between the columnar dendrite boundaries.[5] Solidification cracking can be suppressed using welding consumables with a chemical composition similar to that of the base metal (FMS alloy).[6] However, the total elongation of fillet weld metals decreased remarkably to 26% compared with the base metal (65%). Coarse columnar dendritic grains partially remained on the post-fracture surface of the fillet weld metal owing to A mode solidification, which caused intergranular fracture along the dendrite boundaries. Moreover, the fatigue life of the fillet weld metal (2 560 cycles) was shorter than that of the base metal (approximately 9 000 cycles) at the total strain amplitude of 1% and the strain ratio of −1. This may be attributable to the intergranular fracture between the coarse columnar dendrites.

To improve the susceptibility to solidification cracking and the mechanical properties of the FMS alloy, an FMS alloy solidified in the ferrite-austenite (FA) mode (Fe-15Mn-11Cr-7.5Ni-4Si) was developed by modifying the Cr/Ni equivalent ratio based on the Schaeffler diagram.[5] When the Cr/Ni equivalent ratio calculated using Schaeffler's equations[7] was higher than 1.02, the solidification mode transitioned from A to FA modes. The formation of the primary ferrite phase during solidification in the FA mode is known to suppress the solidification cracking of austenitic stainless steel.[8–10] We demonstrated that the sound weld metal of the FMS alloy solidified in the FA mode was produced by gas metal arc welding[5] even without welding consumable or tungsten inert gas (TIG) welding.[11,12]

In this study, a similar fillet welded joint of an FMS alloy solidified in the FA mode was produced using gas metal arc welding with a welding consumable. A technique for dissimilar welding between an FMS alloy and rolled steel for building structures (SN490B steel) was also developed to join the core part (FMS alloy) to the edge part (SN490B) of the seismic damper. The welding consumables for similar and dissimilar welded joints were designed based on the Schaeffler diagram. The tensile and low-cycle fatigue properties of the similar and dissimilar fillet welded metals were examined. The microstructures of the pre- and post-fracture specimens in the tensile and low-cycle fatigue tests were characterized using electron backscatter diffraction (EBSD).

2. Experimental Procedures

2.1. Materials and Fillet Weld Joint

An ingot with a nominal composition of Fe-15Mn-11Cr-7.5Ni-4Si solidified in the FA mode was prepared by vacuum induction melting, hot-forged at 1 323 K, and rolled into a plate. The plate was annealed at 1 373 K for 1 h and cooled in air. Commercial rolled steel for building structure (SN490B steel) was used. The chemical compositions of the FMS alloy and SN490B steel are listed in **Table 1**. The C content was measured using the infrared absorption method. The contents of the remaining elements were measured by inductively coupled plasma atomic emission spectrophotometry.

Figure 2(a) shows a schematic of the dimensions of the fillet weld joint. The web plate had a length, width, and thickness of 210, 35, and 20 mm, respectively. The flange plate had a length, width, and thickness of 210, 70, and

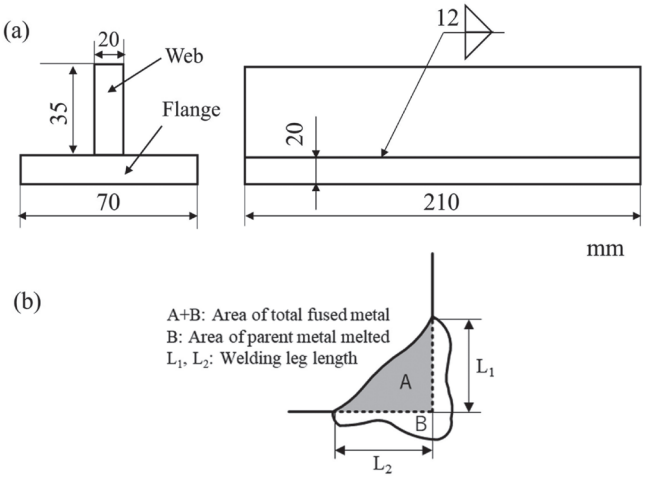

Fig. 2. Schematic presenting (a) dimensions and (b) cross-section of fillet weld joint.

Table 1. Chemical compositions (mass%) of base metal, welding consumables, and fillet weld metals.

	C	Si	Mn	P	S	Cr	Ni	Mo	Nb	Fe	Cr_{eq}	Ni_{eq}
FMS alloy	0.028	4.07	15.40	0.003	0.0032	11.10	7.53	–	0.01	Bal.	17.21	16.07
SN490B steel	0.111	0.25	1.49	0.020	0.0023	0.09	0.07	0.04	–	Bal.	0.51	4.15
Welding consumable 1	0.015	3.91	15.10	0.003	0.0070	11.10	7.79	0.01	0.01	Bal.	16.98	15.79
Welding consumable 2	0.017	3.99	10.20	0.003	0.0080	15.80	7.28	0.01	0.01	Bal.	21.80	12.89
Fillet weld metal 1	0.020	3.93	15.20	0.003	0.0024	11.10	7.73	0.01	0.01	Bal.	17.01	15.93
Fillet weld metal 2	0.023	3.99	12.10	0.003	0.0021	14.20	7.41	0.01	0.01	Bal.	20.20	14.15
Fillet weld metal 3	0.032	3.36	9.01	0.006	0.0019	12.90	6.10	0.01	0.01	Bal.	17.96	11.57

Cr_{eq} = mass%Cr + mass%Mo + 1.5 × mass%Si + 0.5 × mass%Nb
Ni_{eq} = mass%Ni + 30 × mass%C + 0.5 × mass%Mn

20 mm, respectively. Although the core (FMS alloy) and edge parts (SN490B steel) should be joined by butt welding, as shown in Fig. 1, a dissimilar fillet welded joint was produced to compare the microstructure and mechanical properties with those of similar fillet weld metals. In addition, the dilution of the dissimilar fillet welding between the FMS alloy and SM490 steel (20–35%)[6] was almost equivalent to that of the V-shaped dissimilar butt welding (20–30%) between the FMS alloy and low carbon steel.[13] Therefore, the microstructure and mechanical properties of fillet weld metals are considered to be similar to those of butt weld metals. The dissimilar fillet welded joint consisted of an FMS alloy flange plate and SN490B steel web plate. Gas metal arc welding was conducted to produce similar and dissimilar fillet weld joints using welding consumables with a diameter of 1.2 mm. To achieve a welding leg length of 12 mm for similar and dissimilar fillet weld joints, which were required to obtain the tensile and low-cycle fatigue specimens, the arc voltage, welding current, and welding speed were selected as 20 V, 300 A, and 3.3 mm/s, respectively. Argon at a flow rate of 25 L/min was used as the shielding gas. The welding torch was tilted 10° backward in the welding direction. The welding torch was centered on the joint for both similar and dissimilar welds.

An optical microscope (OM) was used to examine the weldability. The microstructures of the pre- and post-fracture specimens in the tensile and low-cycle fatigue tests were characterized using electron backscattering diffraction (EBSD) with an accelerating voltage of 15 kV and a step size of 1–0.08 μm. The grain size was calculated as the circular equivalent diameter of each grain on the EBSD map. The grain boundaries were classified into low angle boundaries (LAB, $2° < \theta < 15°$), high angle boundaries (HAB, $\theta > 15°$), and $\Sigma 3$ twin boundaries (TB). These were determined by the $<111>/60°$ axis/angle pair.

The welding leg length L and dilution D of the fillet weld joint are defined by the following equations:

$$L = (L_1 + L_2)/2 \quad \text{..... (1)}$$

$$D = B/(A+B)\times 100 \quad \text{..... (2)}$$

where L_1 and L_2 are the welding leg lengths on the web and flange sides, respectively; $A + B$ is the total fused metal area; and B is the area of the melted parent metal, as shown in Fig. 2(b).

2.2. Welding Consumable

The welding consumables for the similar and dissimilar fillet welded joints were designed based on the Schaeffler diagram.[14] It can predict the stable phases in the weld metal for austenitic stainless steels. Table 1 shows the actual chemical compositions of the welding consumables. The Cr equivalent (Cr_{eq}) and Ni equivalent (Ni_{eq}) of the FMS alloy, SN490B, and the welding consumables are plotted in **Fig. 3**.

For a similar fillet welded joint, a welding consumable (welding consumable 1) with a chemical composition similar to that of the base metal (FMS alloy) was produced to suppress the dilution of the weld metal. As shown in Table 1 and Fig. 3, the Cr_{eq} and Ni_{eq} values of the FMS alloy are similar to those of welding consumable 1. Notably, the FMS alloy solidified in the FA mode[5] although the Cr/Ni equivalent ratio (= 1.07) exists in the full austenitic region of the Schaeffler diagram.[14]

For the dissimilar fillet welded joint, the chemical composition of the welding consumables (welding consumable 2) was determined according to the following procedure: As shown in Fig. 3(b), the midpoint of the line connecting the chemical compositions of the FMS alloy and SN490B steel corresponds to C. The dilution was within the range of 20–35%, according to our previous studies on dissimilar fillet welding between FMS alloy and SM490 alloy.[6] Therefore, when the chemical composition of welding consumable is determined as the point E, the chemical composition of the weld metal lies along the red line where the formation of α'-martensite degrading the low-cycle fatigue property[2,5,15] does not occur. Notably, E is a limit for manufacturing solid wire because the sigma phase embrittlement occurs[16] in the grey region, as shown in Fig. 3, during heat treatment.

According to the Schaeffler diagram, the amount of primary ferrite during solidification increases with an increase in the Cr/Ni equivalent ratio, which likely influences the solidification microstructure and mechanical properties. A

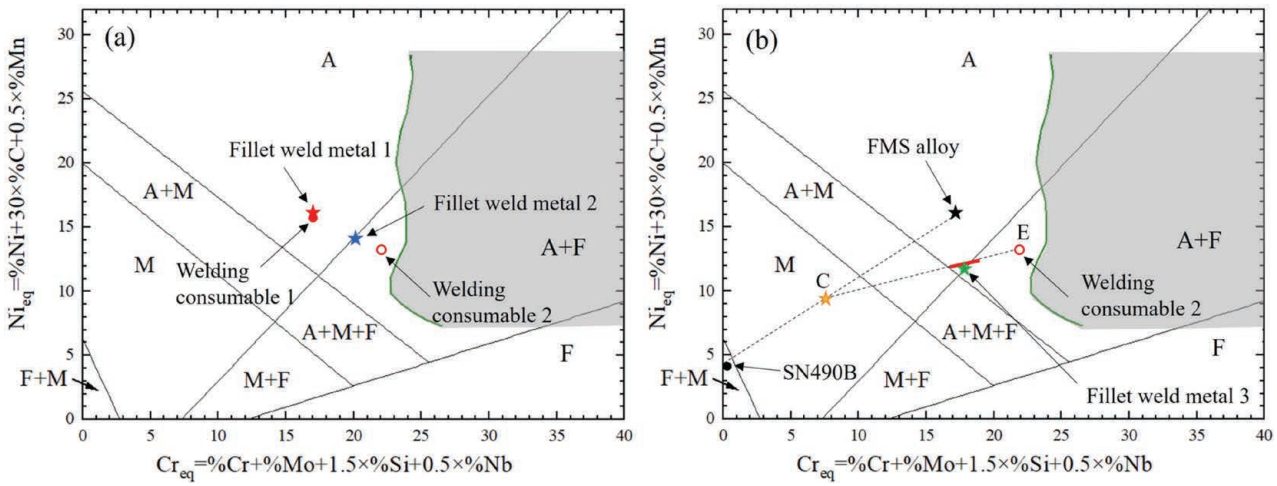

Fig. 3. Schaeffler diagrams showing (a) compositions of fillet weld metals 1 and 2, and welding consumables 1 and 2, and (b) compositions of fillet weld metal 3, FMS alloy, SN490B steel, and welding consumable 2. A, F, and M denote austenite, ferrite, and martensite, respectively. (Online version in color.)

similar fillet welded joint with a high Cr/Ni equivalent ratio was produced using welding consumable 2, which was designed for dissimilar fillet welding. As the Cr/Ni equivalent ratios of the FMS alloy and welding consumable 2 are 1.07 and 1.69, respectively, the Cr/Ni equivalent ratio of the weld metal is likely to lie between these.

2.3. Tensile and Low-cycle Fatigue Tests

Figure 4(a) illustrates a fillet welded joint. All the tensile and low-cycle fatigue specimens were collected from the weld metal of the fillet welded joint. This is indicated by the dotted squares in Fig. 4(a). Figures 4(b) and 4(c) present the dimensions of the tensile and low-cycle fatigue specimens, respectively. The tensile tests were performed at room temperature using an Instron 5982 machine. The load rate was 10 MPa/s until 0.2% proof stress was achieved. From this point, the strain rate was set to 0.5%/s.

Axial strain controlled fatigue tests were conducted using an MTS 370 machine (MTS Systems Corporation). A triangular wave shape was used at a strain rate of 0.4%/s. The strain ratio was −1, and the total strain amplitude was 1%. The tensile and low-cycle fatigue tests were repeated two and three times, respectively, to verify the reproducibility.

3. Result and Discussions

3.1. Similar Fillet Welded Joints

Figures 5(a) and 5(c) display photographs illustrating the appearance of the similar FMS/FMS fillet welded joints produced using welding consumables 1 and 2, respectively. Optical micrographs of the cross-sections of the fillet welded joints produced using welding consumables 1 and 2 are shown in Figs. 5(b) and 5(d), respectively. According to our previous studies on the *in-situ* observation of solidification behaviors at the weld bead of the FMS alloy,[17] the unique FA mode solidification where many equiaxed γ-austenite dendrites appeared in front of the growing columnar δ-ferrite dendrites, occurred at the higher welding speed of 10 mm/s. Simultaneously, the cellular γ-austenite crystals were formed in the interdendritic regions of primary δ-ferrite. When the welding speed decreased below 6 mm/s, the weld pool changed from a teardrop to an elliptical shape. As a result, the columnar dendrites tended to grow in a direction parallel to the welding direction, and γ-austenite equiaxed dendrites were not formed. The formation of cellular γ-austenite crystals occurred only in the interdendritic regions of primary δ-ferrite. This is because the solute enrichment in the melt induced by the impingement of

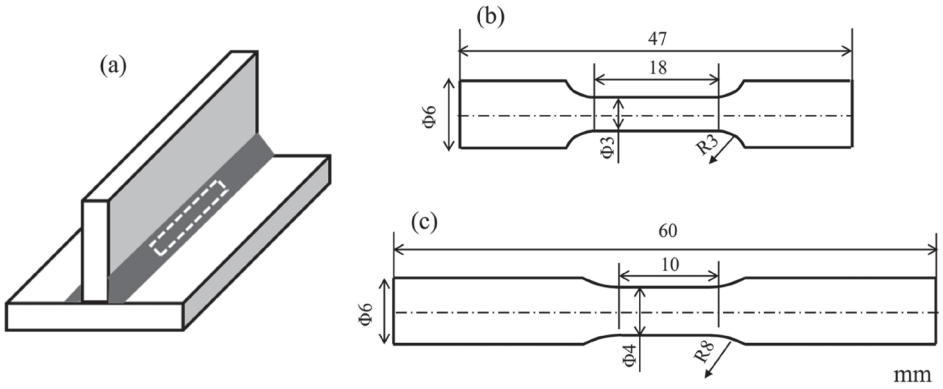

Fig. 4. (a) Illustration of the fillet welded joint, where the dotted square shows the location to collect the tensile and low-cycle fatigue specimens. Dimensions of (a) tensile and (b) low-cycle fatigue specimens.

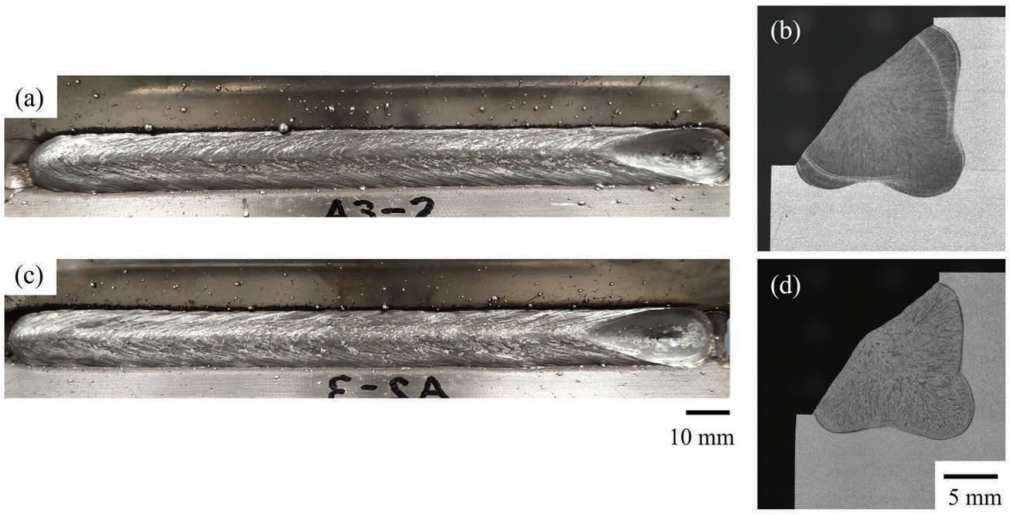

Fig. 5. Photographs illustrating the appearance of the similar FMS/FMS fillet welded joints produced using welding consumables (a) 1 and (c) 2. Optical micrographs of the cross-section of the fillet welded joints produced using welding consumables (b) 1 and (d) 2. (Online version in color.)

columnar dendrites at the center of the weld bead is required to form the equiaxed dendrites.[11,12] In this study, the gas metal arc welding was conducted at the lower welding speed of 3.3 mm/s. In addition, the impingement of columnar grains at the center of the weld bead and the equiaxed grains were not observed, as shown in Figs. 5(b) and 5(d). Therefore, the weld metals are considered to be solidified in the FA mode where the cellular γ-austenite crystals grew independently in the interdendritic regions. Although the equiaxed γ-austenite grains were not formed at the center of the weld bead, sound weld joints were obtained without macro defects for the fillet weld metals. As shown in Table 1, the chemical compositions of sulfur and phosphors which enhance the solidification cracking susceptibility were negligibly low for all the specimens. Therefore, the isolated and discontinuous liquid films likely acted as a resistance to solidification cracking owing to the formation of primary δ-ferrite.[8–10] Notably, the primary δ-ferrite transformed completely into γ-austenite in a solid-state reaction during cooling.[11,12,15] This was unlike the conventional FA mode for austenitic stainless steels.[8,18]

The similar FMS/FMS fillet welded joint produced using welding consumable 1 (fillet weld metal 1) showed a welding leg length of 12.5 mm and dilution of 37.4%. These were calculated using Eqs. (1) and (2), respectively. For the similar FMS/FMS fillet welded joint produced using welding consumable 2 (fillet weld metal 2), the welding leg length and dilution were 11.5 mm and 36.8%, respectively. The actual chemical compositions of fillet weld metals 1 and 2 are listed in Table 1. Their Cr_{eq} and Ni_{eq} values are plotted in Fig. 3(a). Fillet weld metal 1 was produced using welding consumable 1 with a similar chemical composition similar to that of the base metal. Consequently, the chemical composition of the weld metal remained almost unaltered. Meanwhile, fillet weld metal 2 was diluted by welding consumable 2 with a high Cr/Ni equivalent ratio, as shown in Fig. 3(a). The Cr/Ni equivalent ratio was 1.43, as listed in Table 1. The chemical composition of fillet weld metal 2 was almost consistent with the predicted value calculated based on a dilution of 36.8%.

Figures 6(a–c), 6(d–f), and Fig. 6(g–i) show the EBSD results for the FMS alloy and fillet weld metals 1 and 2, respectively. An inverse pole figure (IPF) map; a grain boundary map where the black, green, and red lines denote the HABs, LABs and TBs; and phase maps where green denotes the γ-phase are shown in Figs. 6(a, d, g), 6(b, e, h) and 6(c, f, i), respectively. The FMS alloy exhibited a fully austenitic structure with an average grain size of 67.2 μm. A large number of annealing twin boundaries (57%) were distributed randomly throughout the microstructure owing to the heat treatment during the sample preparation. This is typical characteristic of FCC metals with low stacking fault energy.[19] The fraction of LAB was remarkably low (4%). For fillet weld metals 1 and 2, the microstructures consisted of a fully austenitic structure with columnar grains. This was unlike the polygonal grains of the FMS alloy. The fractions of LAB in fillet weld metals 1 and 2 were 65% and 35%, respectively. These were remarkably higher than that of the FMS alloy owing to the absence of heat treatment (as-weld metal). The average grain size of fillet weld metal 2 with a high Cr/Ni equivalent ratio (163.7 μm) was remarkably larger than that of weld metal 1 (90.7 μm). As the fillet weld metals solidified in the FA mode where the cellular γ-austenite crystals grew independently in the interdendritic regions, the coarser primary δ-ferrite for fillet weld metal 2 was likely formed during solidification owing to the high

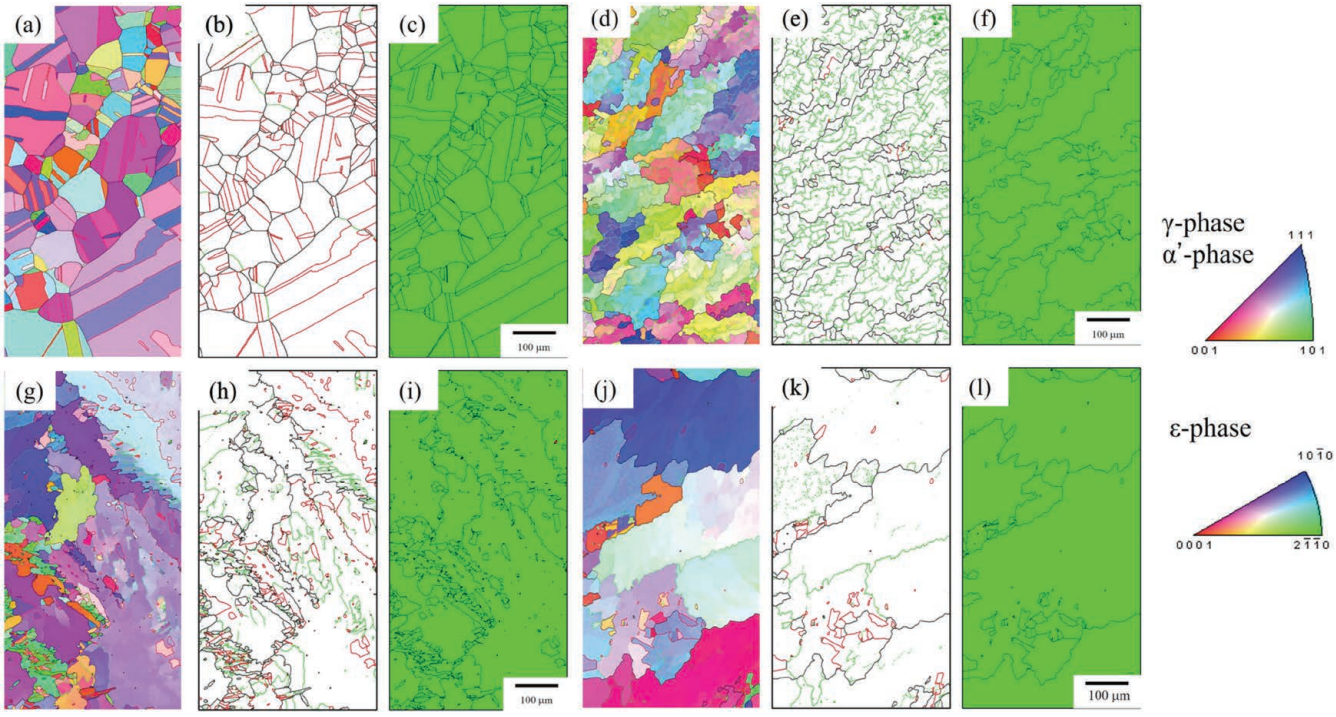

Fig. 6. Microstructures of (a–c) FMS alloy, (d–f) fillet weld metal 1, (g–i) fillet weld metal 2, and (j–l) fillet weld metal 3. (a, d, g, j) IPF map; (b, e, h, k) grain boundary map, where the black, green, and red lines denote the HABs, LABs, and TBs, respectively; and (c, f, i, j) phase map, where green denotes the γ-phase. The step size is 1 μm. (Online version in color.)

Cr/Ni equivalent ratio. As a result, the coarser γ-austenite grains were formed via the solid-state transformation from primary δ-ferrite during cooling.

Figure 7 shows the nominal stress–strain curves of the tensile test for the FMS alloy and fillet weld metals 1 and 2. The results are summarized in **Table 2**. The 0.2% yield stress, tensile strength, and total elongation of FMS alloy were 235 MPa, 691 MPa, and 79%, respectively. Meanwhile, fillet weld metals 1 and 2 showed higher tensile strength (716–736 MPa) and marginally lower total elongation (67–70%) than the FMS alloy. This was notwithstanding that the grain sizes of fillet weld metals 1 and 2 were larger than those of the FMS alloy. SEM images of the fracture surfaces of the tensile specimens of the FMS alloy and fillet weld metals 1 and 2 are shown in **Figs. 8**(a), 8(b), and Fig. 8(c), respectively. The fracture surfaces of all the specimens showed dimple patterns, which was typical ductile fracture surface. The dendrite morphology, which was visible in the weld metal solidified in the A mode for the FMS alloy,[6] was not formed. The FA mode solidification suppressed intergranular fracture.

Figures 9(a, b), 9(c, d), and Fig. 9(e, f) show the post-tensile fracture surface microstructures of the FMS alloy and fillet weld metals 1 and 2, respectively. An IPF map and phase maps where green, yellow, and red denote the γ, ε, and α' phases, respectively, are shown in Figs. 9(a, c, e) and 9(b, d, f), respectively. The image quality deteriorated partially owing to lattice distortion and the introduction of high dislocation during the tensile test. Therefore, images with a confidence index of less than 0.1 were excluded. The textures of γ-austenite for the FMS alloy and fillet weld metals 1 and 2 developed during the tensile test. The orientations of the γ-austenite grains were nearly parallel to the <111> direction with respect to the loading axis. The microstructures of the FMS alloy and fillet weld metals 1 and 2 consisted of γ-austenite, ε-martensite, and α'-martensite. This indicates that the ε- and α'-martensitic transformations occurred during tensile deformation. According to

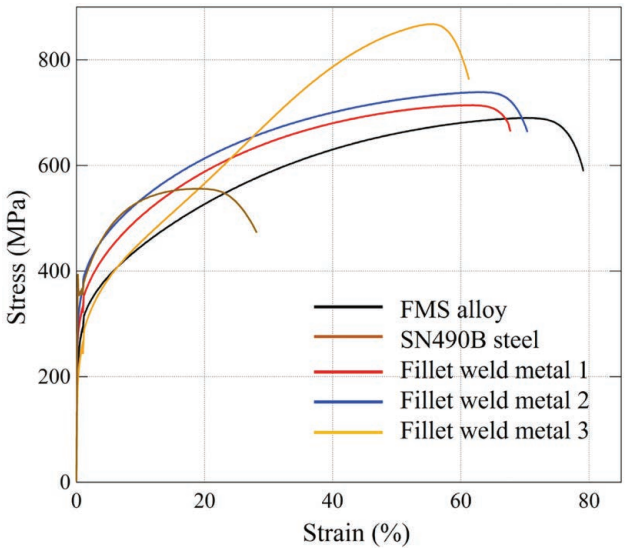

Fig. 7. Nominal stress–strain curves of FMS alloy, SN490B steel, fillet weld metals 1, 2, and 3. (Online version in color.)

Table 2. Results of tensile and low-cycle fatigue tests for the base metals and fillet weld metals.

	0.2% yield stress (MPa)	Tensile strength (MPa)	Total elongation (%)	Number of cycles to fatigue fracture, N_f (cycles)
FMS alloy	235	691	79	9 351
SN490B	358	553	28	–
Fillet weld metal 1	291	716	67	5 740
Fillet weld metal 2	317	736	70	3 789
Fillet weld metal 3	225	867	61	558

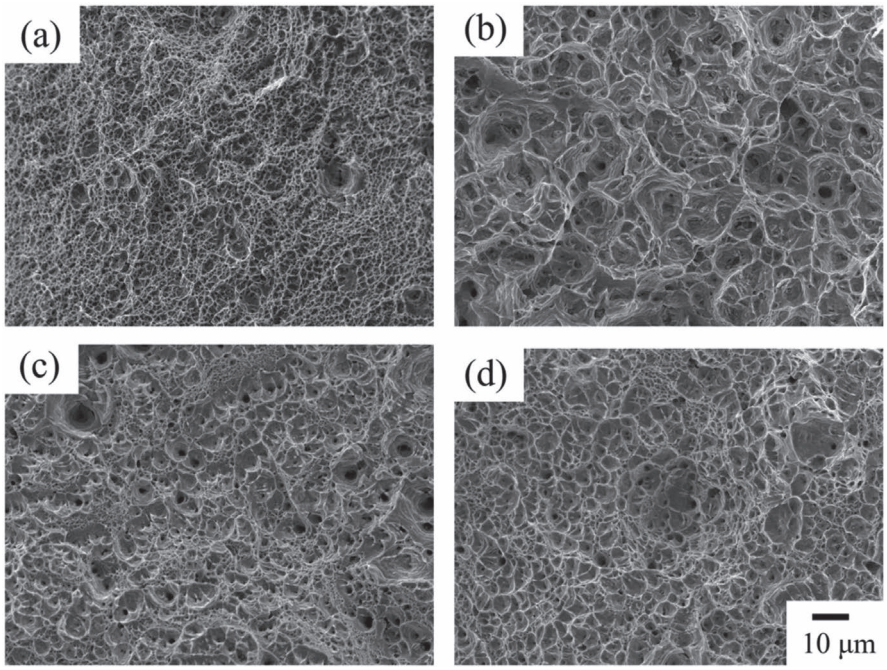

Fig. 8. SEM images of fracture surface of tensile specimens of (a) FMS alloy, (b) fillet weld metal 1, (c) fillet weld metal 2, and (d) fillet weld metal 3.

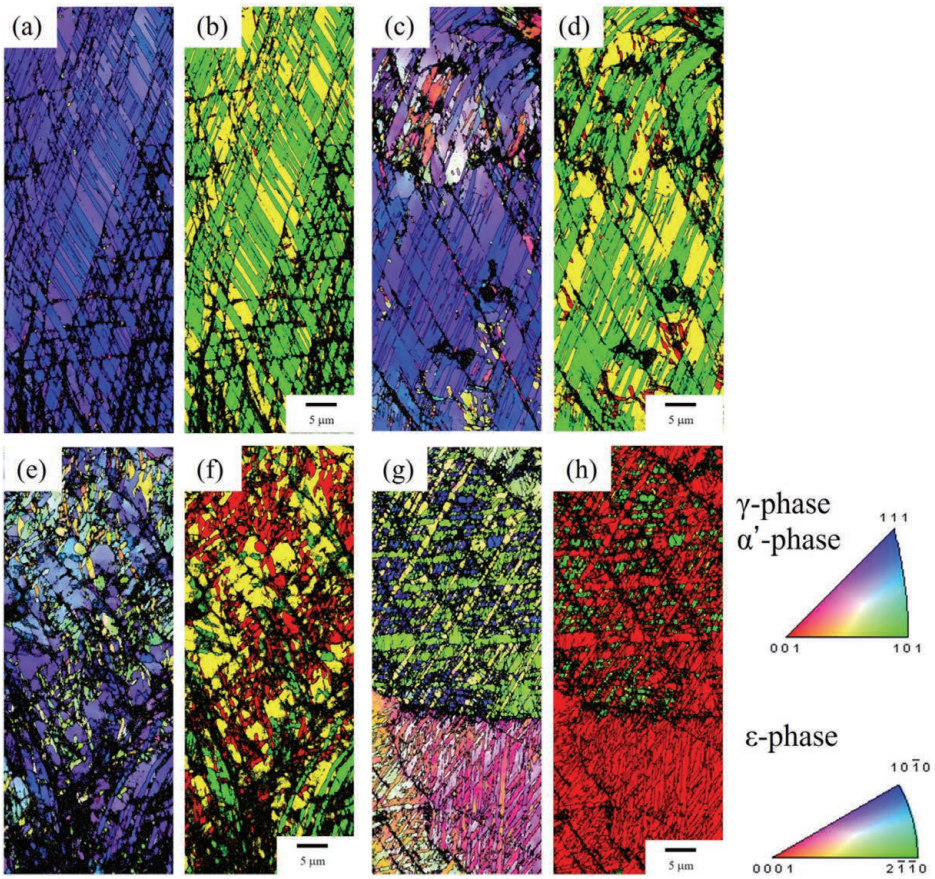

Fig. 9. Post-tensile fracture microstructures of (a, b) FMS alloy, (c, d) fillet weld metal 1, (e, f) fillet weld metal 2, and (g, h) fillet weld metal 3, respectively. (a, c, e, g) IPF map and (b, d, f, h) phase map, where green, yellow, and red denote the γ, ε, and α' phases, respectively. The step size is 0.08 μm. (Online version in color.)

the previous studies on the tensile deformation behaviors of the FMS alloy, α'-martensite was formed through the two-stage $\gamma \rightarrow \varepsilon \rightarrow \alpha$' transformation.[20] The strain-induced ε-martensitic and α'-martensitic transformation caused the increase in the work hardening rate. This, in turn, enhanced the ductility of fillet meld metals 1 and 2 as well as the FMS alloy, as shown in Fig. 7. For the FMS alloy and fillet weld metals 1 and 2, the amounts of ε-martensite were 28.5%, 30.5%, and 22.4%, whereas those of α'-martensite were 0.8%, 2.6%, and 13.9%, respectively. This indicates that the strain-induced α'-martensitic transformation occurred frequently for the fillet weld metals. Therefore, the higher tensile strength of the fillet weld metal than that of the FMS alloy was attributed to the higher amount of α'-martensite.

Figures 10(a) and 10(b) show the stress–strain hysteresis loops, where the dashed and solid lines denote first cycle and half-life cycle, and cyclic hardening curves during the fatigue test, respectively, for the FMS alloy and fillet weld metals 1 and 2. The hysteresis loops of all the specimens remained almost unaltered after the half-life cycle owing to the quite gradual cyclic hardening shown in Fig. 10(b). The peak stress of all the specimens increased gradually with an increase in the number of cycles. In general, an FMS alloy undergoes cyclic hardening owing to the increase in the amount of ε-martensite via the gradual growth of ε-martensite and accumulation of dislocations in the ε-martensite, caused by the reversible martensitic transformation.[20] The peak stress of the fillet weld metal is higher than that of the FMS alloy over all the cycles, as shown in Fig. 10(b). The fatigue life, N_f of the FMS alloy and fillet weld metals 1 and 2 are listed in Table 2. Fillet weld metal 1 showed a remarkable N_f (5 740 cycles), which increased by approximately two times from that of the fillet weld metal solidified in A mode (2 560 cycles).[6] Fillet weld metal 2 retained a long N_f (3 789 cycles) even at a high Cr/Ni equivalent ratio.

According to the previous studies,[21] the N_f of the FMS alloy depends on the thermodynamic phase stability between γ and ε, which is determined by the Gibbs free energy difference ($\Delta G^{\gamma \rightarrow \varepsilon}$). To achieve the reversible transformation from γ-austenite to ε-martensite, the $\Delta G^{\gamma \rightarrow \varepsilon}$ of the FMS alloy was set to approximately 0 J/mol. Here, N_f attained the maximum value,[19] and it decreased with a decrease in $\Delta G^{\gamma \rightarrow \varepsilon}$ in the negative direction. In this study, $\Delta G^{\gamma \rightarrow \varepsilon}$ was calculated to be -56.9, -52.7, -41.9 J/mol for the FMS alloy and fillet meld metals 1 and 2, respectively, based on the chemical composition shown in Table 1. The detailed calculation method for $\Delta G^{\gamma \rightarrow \varepsilon}$ is shown in Reference 20. The long N_f of the fillet weld metals is attributed to its nearly desirable $\Delta G^{\gamma \rightarrow \varepsilon}$, which was almost equivalent to that of the FMS alloy.

Figures 11(a, b), 11(c, d), and Fig. 11(e, f) show the post-fatigue microstructures of the FMS alloy and fillet weld metals 1 and 2, respectively. The IPF and phase maps are shown in Figs. 11(a, c, e) and 11(b, d, f), respectively. For all the specimens, the plate-like morphology in the ε-martensite was highly developed because of the cyclic deformation. This is typical characteristics for the FMS

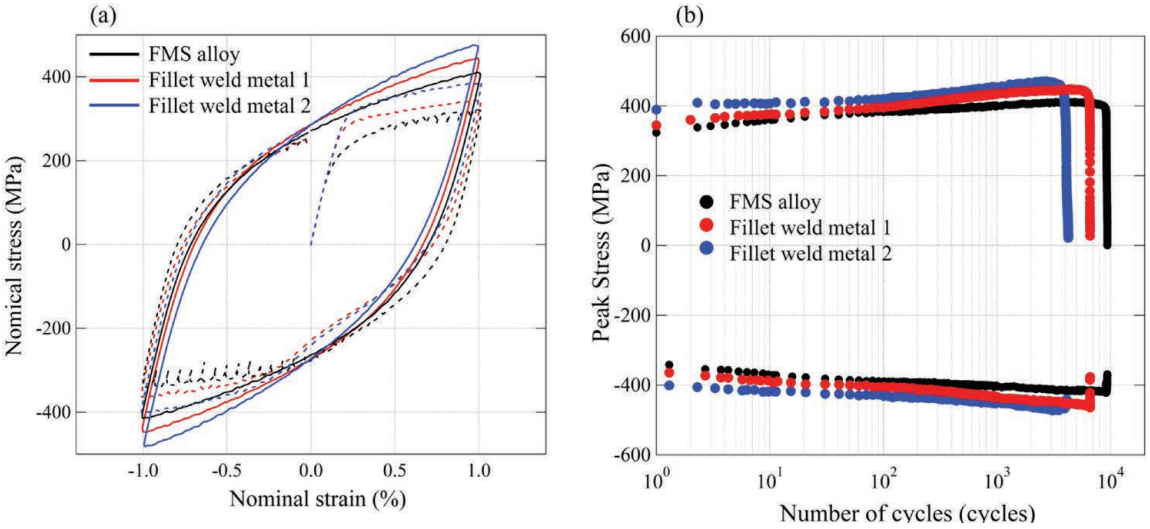

Fig. 10. (a) Stress–strain hysteresis loops for the FMS alloy and fillet weld metals 1 and 2. Dashed and solid lines denote first cycle and half-life cycle, respectively. (b) Cyclic hardening curves during low-cycle fatigue test for the FMS alloy and fillet weld metals 1 and 2. (Online version in color.)

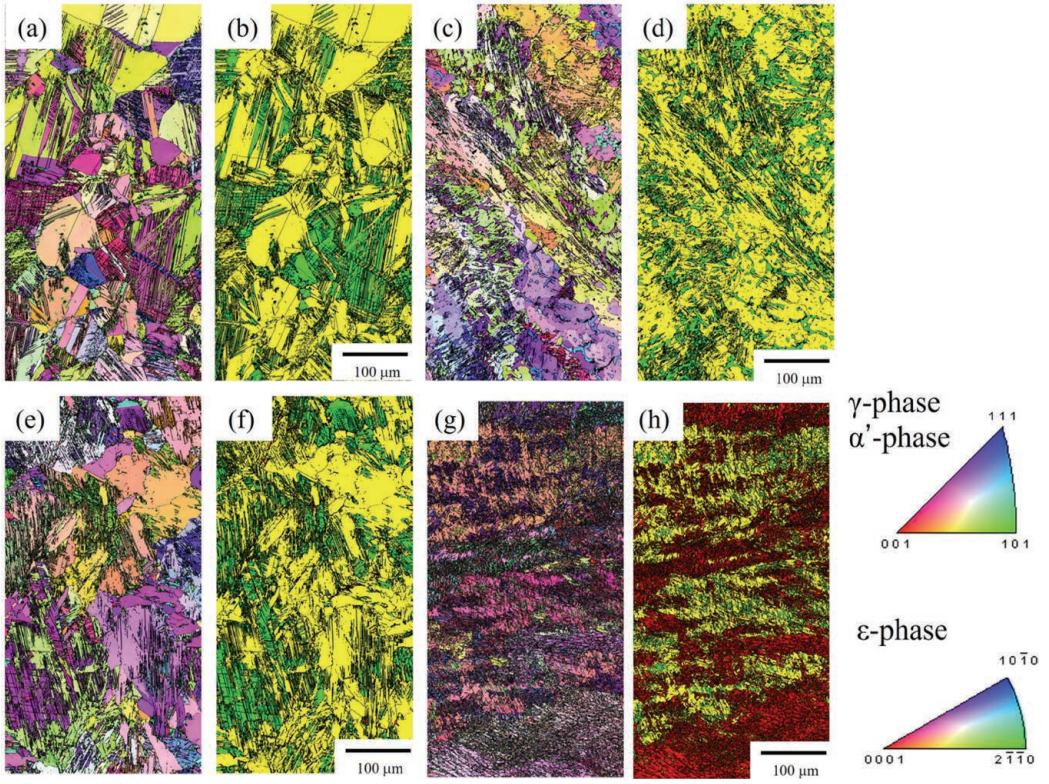

Fig. 11. Post-fatigue microstructures of (a, b) FMS alloy, (c, d) fillet weld metal 1, (e, f) fillet weld metal 2, and (g, h) fillet weld metal 3, respectively. (a, c, e, g) IPF map and (b, d, f, h) phase map, where green, yellow, and red denote the γ, ε, and α' phases, respectively. The step size is 0.5 μm. (Online version in color.)

alloy.[2] The microstructure of the FMS alloy consisted of γ-austenite (26.7%), a large amount of ε-martensite (72.5%), and a small amount of α'-martensite (0.9%). The dominant part of γ-phase transitioned to ε-martensite during the fatigue test. Similarly, fillet weld metal 1 consisted of γ-austenite (26.7%), ε-martensite (73.2%) and α'-martensite (1.1%), and fillet weld metal 2 consisted of γ-austenite (25.7%), ε-martensite (71.4%), and α'-martensite (2.6%). The α'-martensitic transformation is irreversible.[2,5,15,22] The previous study on other FMS alloy proposed that the formation of α'-martensite reduces the chance of occurrence of the reversible transformation from γ-austenite to ε-martensite, which causes the degradation of N_f.[15] In this study, therefore, the easier formation of α'-martensite in fillet weld metal compared with the base FMS alloy may decrease N_f. This is shown in Fig. 10 and Table 2.

In our previous studies,[23] friction stir welding (FSW; a solid-state joining technique) was applied to an FMS alloy (Fe-15M-10Cr-8Ni-4Si) to examine its weldability. An FSW joint with a 10 mm-thick plate was obtained without macro defects. The stir zone of the FSW specimen exhibited a fine microstructure consisting of full γ-austenite

grains with a diameter of 18.6 μm and a longer N_f (9 723 cycles) than the base metal (8 908 cycles). Furukane *et al.*[24] reported the effect of γ-austenite grain-size within 10–30 μm on the strain-induced α'-martensitic transformation rate for the austenitic stainless steel (SUS316L). The decrease in grain size of γ-austenite hindered the strain-induced α'-martensitic transformation. Therefore, this transformation was suppressed by the grain refinement of γ-austenite, which resulted in the improvement of the N_f for the stir zone of the FSW specimen. These results indicate that the strain-induced α'-martensitic transformation occurred more frequently for the fillet weld metal with coarse γ-austenite grains. This yielded the higher tensile strength and higher peak stress of the cyclic hardening curve. Moreover, the N_f values of the fillet weld metals were shorter than that of the FMS alloy.

Mn stabilizes γ-austenite and suppresses the α'-martensitic transformation that occurs in Fe–Mn alloys under fatigue loadings.[25,26] Therefore, the Mn content is generally set to over 15% for the FMS alloys with a long fatigue life.[2] The Mn content of fillet weld metal 2 was 12%, as shown in Table 1. Thus, the strain-induced α'-martensitic transformation was enhanced by the low Mn content and the large grain size of γ-austenite for fillet weld metal 2. This yielded an N_f value shorter than those of fillet weld metal 1 and the FMS alloy.

In the case of the higher welding speed, the formation of equiaxed γ-austenite grains at the center of weld bead is expected owing to the unique FA mode. The effect of the equiaxed γ-austenite grains on the mechanical properties is future subject.

3.2. Dissimilar Fillet Welded Joint

Figures 12(a) and 12(b) show photographs illustrating the appearance and optical micrograph of the cross-section of the dissimilar FMS/SN490B fillet welded joint produced using welding consumable 2 (fillet weld metal 3). A sound weld joint with a welding leg length of 12.4 mm and dilution of 24.0% was obtained without macro defects. The actual chemical composition of fillet weld metal 3 is listed in Table 1. Cr_{eq} and Ni_{eq} values are plotted in Fig. 3(b). The measured dilution was within the anticipated range, as shown in Section 2.2. The chemical composition lay in the austenite region without α'-martensite. Figures 6(j), 6(k) and 6(l) show the IPF, grain boundary, and phase maps, respectively, of fillet weld metal 3. Fillet weld metal 3 showed the full austenite microstructure consisting of coarse columnar grains of 266 μm. Because the Cr/Ni equivalent ratio of fillet weld metal 3 (1.55) is higher than that of fillet weld metal 2 (1.42), as shown in Table 1, the larger amount of primary ferrite yielded coarser columnar grains compared with the fillet weld metal 2 (163.7 μm). As in the case of the similar fillet weld metals, the impingement of columnar grains at the center of the weld bead and the equiaxed grains were not observed, as shown in Fig. 12(b). This indicates that the cellular γ-austenite crystals were formed independently in the interdendritic regions of primary δ-ferrite, followed by the solid-state transformation from primary δ-ferrite to γ-austenite.

The nominal stress–strain curve and the results of the tensile test performed on fillet weld metal 3 are shown in Fig. 7 and Table 2, respectively. The nominal stress was similar to that of the FMS alloy up to 10% strain. Above this, it increased remarkably and attained 867 MPa. This was higher than those of the FMS alloy and fillet weld metals 1 and 2 notwithstanding the largest austenite grains. Meanwhile, fillet weld metal 3 showed a high total elongation of 60%. This is comparable to that of similar fillet weld metals (67–70%). Figure 8(d) shows the SEM image of the fracture surface of the tensile specimen of fillet weld metal 3. The dimple patterns were observed owing to the FA mode solidification. This was similar to case of the FMS alloy and similar fillet weld metals.

Figures 9(g) and 9(h) show the IPF and phase maps, respectively, of the post-tensile fracture surface microstructures of fillet weld metal 3. The microstructure consisted of γ-austenite (3.3%), ε-martensite (2.1%), and a large amount of α'-martensite (54.8%). Notably, the remaining phase was removed because of its low confidence index (< 0.1). The result indicates that the remarkable increase in the stress can be attributed to the frequent occurrence of α'-martensitic transformation.

The core part consisting of FMS alloy plates exhibits a damping effect via its elastoplastic deformation[1] in the proposed brace-type seismic damper, as shown in Fig. 1. Thus, the edge part consisting of SN490B steel plates and dissimilar FMS/SN490B welded joints undergo only elastic deformation. Fillet weld metal 3 exhibited sufficient tensile properties in the elastic deformation range, as shown in Fig. 7. The plastic fatigue performance is not required for dissimilar weld joints. However, it is worthwhile to examine the effect of α'-martensite on the low-cycle fatigue life. This is because the α'-martensitic transformation is most likely to occur during cyclic deformation according to the

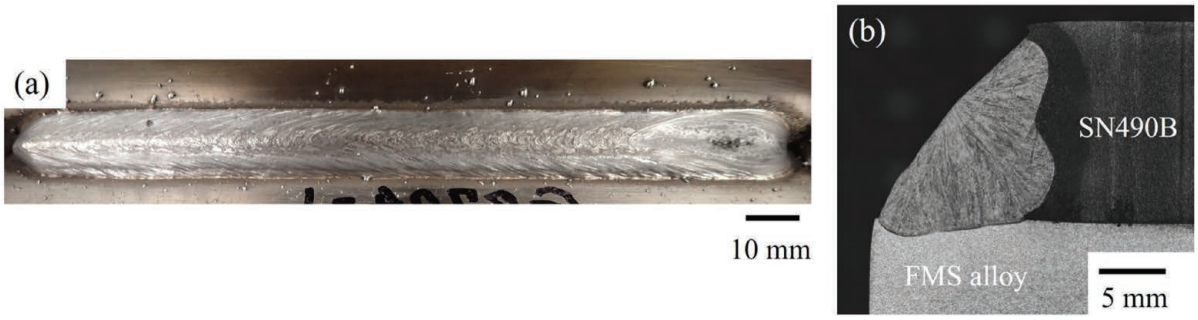

Fig. 12. (a) Photograph illustrating the appearance and (b) optical micrograph of the cross-section of the dissimilar FMS/SN490B fillet welded joint produced using welding consumable 2. (Online version in color.)

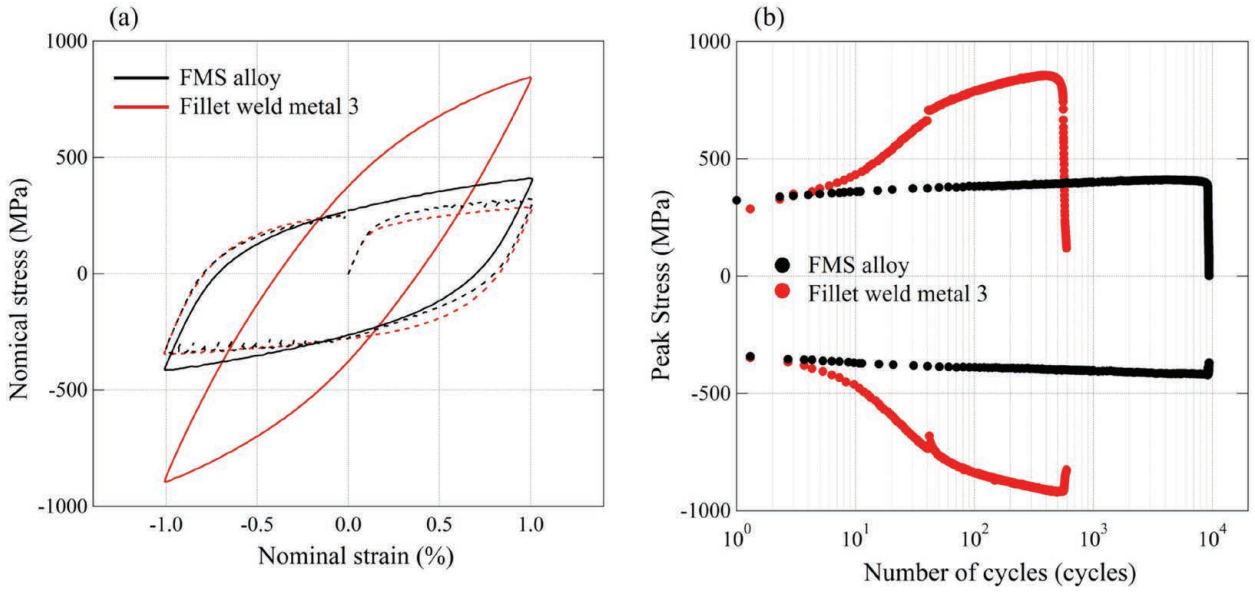

Fig. 13. (a) Stress–strain hysteresis loops for the FMS alloy and fillet weld metal 3. Dashed and solid lines denote first cycle and half-life cycle, respectively. (b) Cyclic hardening curves during low-cycle fatigue test for the FMS alloy and fillet weld metal 3. (Online version in color.)

post–tensile fracture microstructure, as shown in Fig. 9. **Figures 13**(a) and 13(b) show the stress-strain hysteresis loops and cyclic hardening curves during the low-cycle fatigue test, respectively, for the FMS alloy and fillet weld metal 3. The hysteresis loop shape of fillet weld metal 3 at the half-life cycle varied significantly owing to the increase in the nominal stress. This was unlike that for the FMS alloy, as shown in Fig. 13(a). Fillet weld metal 3 initially showed a peak stress of 350 MPa, which is similar to that of the FMS alloy. The peak stress increased remarkably after approximately 10 cycles and attained 850 MPa immediately before fracture. The remarkable increase in stress was similar to the stress–strain curve of the tensile test, as shown in Fig. 7. Fillet weld metal 3 showed an exceptionally short N_f (558 cycles) compared with that for the FMS alloy, as shown in Table 2. As mentioned in Section 3.1, N_f depended on the thermodynamic stability between γ and ε phases. The $\Delta G^{\gamma\to\varepsilon}$ was calculated to be −120.4 J/mol. This was significantly lower than that of the FMS alloy (−56.9 J/mol). The FMS alloys exhibits ε-martensitic transformation via strain-induced mechanism, where ε-martensite grows gradually.[21] However, when $\Delta G^{\gamma\to\varepsilon}$ is quite lower compared with that of FMS alloy, stress-assisted ε-martensitic transformation becomes possible, leading the rapid growth of ε-martensite.[21] Then, the fatigue damage mitigation mechanism owing to the reversible transformation from γ-austenite to ε-martensite is no longer activated, resulting in the decrease in N_f. Figures 11(g) and 11(h) show the IPF and phase maps of the post-fatigue microstructure of fillet weld metal 3, respectively. The fractions of γ-austenite, ε-martensite, and α'-martensite for fillet weld metal 3 were 6.1, 39.0, and 45.0%, respectively. A small amount of γ-austenite existed in the fracture surface. This indicates that most of the γ-austenite transformed rapidly into ε-martensite owing to the low $\Delta G^{\gamma\to\varepsilon}$. Moreover, the α'-martensitic transformation occurred straightforwardly owing to the low amount of Mn (9.01%), which was the stabilizer of γ-austenite and the larger grain size of γ-austenite as in the case of fillet weld metal 2. The rapid growth of ε-martensite and the frequent occurrence of α'-martensitic transformation caused the remarkable decrease in N_f.

4. Conclusions

Gas metal arc welding was applied to produce similar FMS/FMS and dissimilar FMS/SN490B fillet weld joints using welding consumables designed based on the Schaeffler diagram. The tensile and low-cycle fatigue properties of the FMS alloy, similar fillet weld metal, and dissimilar fillet weld metal were examined. The microstructures of the pre- and post-fracture specimens in the tensile and low-cycle fatigue tests were characterized to examine the factors influencing their mechanical properties. The following conclusions were drawn:

(1) For the similar FMS/FMS fillet weld metals produced using the two types of welding consumables with different Cr/Ni equivalent ratios, sound similar fillet welded joints were produced without solidification cracking although both the fillet weld metals showed a full austenitic structure with coarse columnar grains. These exhibited the tensile strength (716–736 MPa) and total elongation (67–70%) similar to those of the FMS alloy. The N_f value of fillet weld metal 1 (5 740 cycles) solidified in FA mode was remarkably improved using the developed welding consumable. The long N_f is attributed to the high $\Delta G^{\gamma\to\varepsilon}$ where strain-induced ε-martensitic transformation occurred. For fillet weld metal 2 with a high Cr/Ni equivalent ratio, the irreversible α'-martensitic transformation caused the marginal decrease in N_f (3 789 cycles) owing to the low Mn content and large grain size of γ-austenite.

(2) For dissimilar FMS/SN490B fillet welding, the chemical composition of the welding consumables was determined such that the chemical composition of the weld metal was in the austenite region of the Schaeffler diagram. A sound dissimilar fillet welded joint with a dilution of 24.0% was produced without α'-martensite. The dissimilar

fillet weld metal showed sufficient tensile properties including higher tensile strength (867 MPa) and total elongation (61%). N_f decreased remarkably because of the low $\Delta G^{\gamma\rightarrow\varepsilon}$ and frequent occurrence of α'-martensitic transformation.

Acknowledgments

This study was based on the results obtained from the Adaptable and Seamless Technology Transfer Program through Target-driven R&G (A-STEP) from the Japan Science and Technology Agency (grant no. JPMJTR203B). The study was partially supported by the Japan Society for the Promotion of Science, KAKENHI (grant no. 23H0173).

REFERENCES

1) Y. Inoue, A. Kushibe, K. Umemura, Y. Mizushima, T. Sawaguchi, T. Nakamura, H. Otsuka and Y. Chiba: *Jap. Architect. Rev.*, **4** (2021), 76. https://doi.org/10.1002/2475-8876.12193
2) T. Sawaguchi, I. Nikulin, K. Ogawa, K. Sekido, S. Takamori, T. Maruyama, Y. Chiba, A. Kushibe, Y. Inoue and K. Tsuzaki: *Scr. Mater.*, **99** (2015), 49. https://doi.org/10.1016/j.scriptamat.2014.11.024
3) I. Nikulin, T. Sawaguchi, A. Kushibe, Y. Inoue, H. Otsuka and K. Tsuzaki: *Int. J. Fatigue*, **88** (2016), 132. https://doi.org/10.1016/j.ijfatigue.2016.03.021
4) I. Nikulin, N. Nagashima, F. Yoshinaka and T. Sawaguchi: *Mater. Lett.*, **230** (2018), 257. https://doi.org/10.1016/j.matlet.2018.07.123
5) F. Yoshinaka, T. Sawaguchi, S. Takamori, T. Nakamura, G. Arakane, Y. Inoue, S. Motomura and A. Kushibe: *Scr. Mater.*, **197** (2021), 113815. https://doi.org/10.1016/j.scriptamat.2021.113815
6) T. Nakamura and T. Sawaguchi: *J. Struct. Eng.*, **67B** (2021), 633.
7) P. Guiraldenq and O. Hardouin Duparc: *Metall. Res. Technol.*, **114** (2017), 613. https://doi.org/10.1051/metal/2017059
8) T. Takalo, N. Suutala and T. Moisio: *Metall. Trans. A*, **10a** (1979), 1173. https://doi.org/10.1007/BF02811663
9) P. Yu, K. J. Thompson, J. McCarthy and S. Kou: *Weld. J.*, **97** (2018), 301s. https://doi.org/10.29391/2018.97.026
10) F. Matsuda, H. Nakagawa, I. Kato and Y. Murata: *Trans. JWRI*, **8** (1986), 105.
11) T. Nagira, T. Nakamura, F. Yoshinaka, T. Sawaguchi, Y. Aoki, M. Kamai, H. Fujii, A. Takeuchi and M. Uesugi: *Scr. Mater.*, **216** (2022), 114743. https://doi.org/10.1016/j.scriptamat.2022.114743
12) T. Nagira, T. Nakamura, T. Kimura, F. Yoshinaka, T. Sawaguchi, T. Yamashita, Y. Aoki and H. Fujii: *Q. J. Jpn. Weld. Soc.*, **41** (2023), 1s. https://doi.org/10.2207/qjjws.41.1s
13) The small and medium enterprise angency (Strategic Foundational Technology Improvement Support Operation progress report, 2014), (March, 2014), https://www.chusho.meti.go.jp/keiei/sapoin/portal/seika/2011/23152817144.pdf, (accessed 2023-04-05).
14) A. L. Schaeffler: Data Sheet 680-B, *Met. Prog.*, **56** (1949), 680.
15) F. Yoshinaka, T. Sawaguchi, S. Takamori, S. Emura and Y. Inoue: *Inter. J. Fatigue*, **171** (2023), 107581. https://doi.org/10.1016/j.ijfatigue.2023.107581
16) F. Matsuda: Data Book for Welding and Joining Technologies, Welding Technology Information Center, (2007), 509.
17) T. Nagira, T. Nakamura, F. Yoshinaka, T. Sawaguchi, Y. Aoki, T. Yamashita and H. Fujii: Abstract for the Autumn National Conference of the Japan Welding Society 111, (2022), 198 (in Japanese). https://doi.org/10.14920/jwstaikai.2022f.0_198
18) H. Inoue and T. Koseki: *Acta Mater.*, **124** (2017), 430. https://doi.org/10.1016/j.actamat.2016.11.030
19) J. Humphreys, G. S. Rohrer and A. Rollett: Recrystallization and Related Annealing Phenomena, 3rd ed., Elsevier, Oxford, (2017), 261.
20) F. Yoshinaka, T. Sawaguchi, S. Takamori and S. Emura: *Mater. Sci. Eng. A*, **833** (2022), 142583. https://doi.org/10.1016/j.msea.2021.142583
21) T. Sawaguchi, I. Nikulin, K. Ogawa, S. Takamori, F. Yoshinaka, Y. Chiba, H. Otsuka, Y. Onoue and A. Kushibe: *Acta Mater.*, **220** (2021), 117267. https://doi.org/10.1016/j.actamat.2021.117267
22) F. Yoshinaka, Y. Tsutumi, T. Nagira, S. Takamori, S. Emura, T. Sawaguchi, H. Katayama, T. Nakamura, Y. Inoue, S. Motomura and A. Kushibe: *ISIJ Int.*, **64** (2024), 1197. https://doi.org/10.2355/isijinternational.ISIJINT-2023-437
23) T. Nagira, T. Nakamura, T. Sawaguchi, M. Mori, Y. Morisada and H. Fujii: *ISIJ Int.*, **63** (2023), 2056. https://doi.org/10.2355/isijinternational.ISIJINT-2023-305
24) S. Furukane and S. Torizuka: *Tetsu-to-Hagané*, **105** (2019), 827 (in Japanese). https://doi.org/10.2355/tetsutohagane.TETSU-2019-004
25) X. Li, L. Chen, Y. Zhao and R. D. K. Misra: *Mater. Des.*, **142** (2018), 190. https://doi.org/10.1016/j.matdes.2018.01.026
26) X. Zhang, T. Sawaguchi, K. Ogawa, F. Yin and X. Zhao: *J. Alloy. Comp.*, **577S** (2013), S533. https://doi.org/10.1016/j.jallcom.2011.12.109